

Evidence for the suppression of the hybrid skin-topological effect by fragile topology

Tian-Rui Liu^{1,†}

¹ Key Laboratory of Artificial Micro- and Nano-structures of Ministry of Education and School of Physics and Technology, Wuhan University, Wuhan 430072, China

Corresponding E-mail: [†] tianruiliu@whu.edu.cn

Abstract

Topological insulators are well-known for their topological edge states, which are protected by the non-trivial bulk topology and characterized by gapless Wannier bands, a phenomenon known as the bulk-boundary correspondence. However, fragile topology challenged this concept, the Wannier bands are gapped, but the edge states still exist with similar protection. Previous studies on fragile topology have primarily focused on the spectral flow under twisted boundary conditions, but the discussion on the physical interpretation of the Wannier gap is limited. In this study, we introduce a bilayer breathing honeycomb lattice with spiral interlayer couplings inside the unit cell. As we increase the interlayer coupling strength, the Wannier gap increases monotonically and the bandgap first increases then decreases. After introducing a gain-loss domain wall, the hybrid skin-topological effect (HSTE) emerges, and the topological edge states under the periodic boundary condition (PBC) change into corner states under the open boundary condition (OBC) associated with the significant spectral difference. HSTE is suppressed as the interlayer coupling strength increases, the spectral difference between the two boundary conditions has an overall decreasing trend, which more closely mirrors the evolution of the inverse of the Wannier gap. Moreover, some of the corner states transform into edge states. Our work first provides evidence for the relation between fragile topology and HSTE, shedding new insights into the underlying mechanism of Non-Hermitian skin effect (NHSE).

Introduction

Topological insulators [1–9] have garnered considerable interest over several decades. The non-trivial bulk topology leads to gapless edge states with topological protection, known as bulk-boundary correspondence. However, fragile topology [10–15] presents a challenge to the conventional bulk–boundary correspondence. Fragile topology usually appears in systems without intrinsic fermion time-reversal symmetry, such as topological crystalline insulators [13–17]. The Wannier bands of those crystals are gapped, which means the bulk topology is not non-trivial. However, the edge states still exist, although they may not be gapless, and still present protection and robustness against disorder and bends in various experimental platforms [18–23]. The observable phenomenon of fragile topology focuses on the eigenvalues, the spectral flow under twisted boundary conditions [15–17]. On the contrary, the physical interpretation of the Wannier gap remains unknown, and the property of the eigenstates under fragile topology is still under debate. A representative example is provided by the Wu-Hu model [18–26], also known as the breathing honeycomb lattice, which realizes fragile topology. The debate centers on the topological protection of the edge states, an issue that remains unsettled [25–28]. Thus, it is important to characterize fragile topology from the perspective of eigenstates and to provide a physical interpretation of the Wannier gap.

Non-Hermitian physics [29–37] has attracted growing interest in recent years. Non-Hermitian skin effect (NHSE) [38–49] is a characteristic phenomenon in Non-Hermitian systems with no Hermitian counterpart. For systems exhibiting NHSE, d -dimensional states under the periodic boundary condition (PBC) will at least change into $(d-1)$ -dimensional states under the open boundary condition (OBC). Moreover, the spectra between PBC and OBC also have a significant difference. The hybrid skin-topological effect (HSTE) [50–58] is a newly discovered phenomenon about the NHSE for the topological edge states. For a 2D topological insulator with HSTE, the topological edge states under half-PBC will change into corner states under OBC. In this manuscript, we present evidence suggesting a potential relationship between fragile topology and the suppression of HSTE by introducing a bilayer breathing honeycomb lattice with spiral interlayer couplings [14,17,59–62] that are intracell. The coupling strength is connected to the width of the Wannier gap and the bandgap. When the coupling strength increases, the Wannier gap increases monotonically, and the bandgap first increases then decreases. After introducing a gain-loss domain

wall [55–57,63,64], HSTE emerges, and a significant spectral difference is observed between PBC and OBC. As the interlayer coupling strength increases, that difference exhibits an overall decreasing trend, more closely mirroring the evolution of the inverse of the Wannier gap than the evolution of the bandgap, providing evidence for the connection between fragile topology and the suppression of HSTE. Our findings offer possible characteristics of fragile topology from the perspective of Non-Hermitian systems.

We first introduce the bilayer breathing honeycomb lattice model [14,17,59,60], as shown in Fig. 1(a) and (b). Each layer represents a Wu-Hu model [18–25] with the nearest-neighbor couplings and equalized coupling strength. The following discussions choose the shapes of boundaries along both directions in Fig. 1(a) as armchair boundaries. The two lattice vectors, $\vec{a}_1 = (1,0)$ and $\vec{a}_2 = (1/2, \sqrt{3}/2)$, represent the directions along which the unit cell extends. The interlayer couplings are 120-degree chiral channels [14,17,59,60], acting as a Kane-Mele-like model [9] with real couplings. However, unlike the settings in previous studies [14,17,59,60], the interlayer couplings are only intracell. The gain-loss domain wall [55–57,63,64] is inserted into the system in Fig. 1 (a), and the Hamiltonian is written as,

$$H = t \sum_{\langle m,n \rangle \alpha} a_{m\alpha}^\dagger a_{n\alpha} + \lambda \sum_{\langle\langle m,n \rangle\rangle, \alpha \neq \beta} v_{mn,\alpha} a_{m\alpha}^\dagger a_{n\beta} + i \sum_{m,\alpha} \gamma_m a_{m\alpha}^\dagger a_{m\alpha}. \quad (1)$$

In Eq. (1), $a_{m\alpha}^\dagger (a_{m\alpha})$ represent the annihilation (creation) operators on the m^{th} site ($m = 1, 2, \dots, N_{\text{total}}$) of a single layer, where $\alpha = \uparrow, \downarrow$ represent the upper/lower layers and N_{total} represents the number of total sites of a single layer. The first term is the intralayer nearest-neighbor couplings with the same coupling strength $t = 1$. The second term represents the interlayer and intracell couplings with coupling strength λ . The coefficient $v_{mn,\alpha} = [\epsilon_\alpha (\hat{e}_{lm} \times \hat{e}_{nl})_z + 1]/2$. Here, $\epsilon_{\uparrow\downarrow} = \pm 1$, m and n represent the next-nearest-neighbor sites sharing the same nearest neighbor l and the same unit cell. And \hat{e}_{lm} is a unit vector pointing from l to m and projecting onto the xOy plane. Thus, the interlayer couplings reflect clockwise chirality, as shown in Fig. 1(b). The third term represents the gain-loss domain wall, γ_m is the gain-loss coefficient. For the red sites in Fig. 1(a), $\gamma_m = \gamma \geq 0$, and for the blue sites in Fig. 1(a), $\gamma_m = -\gamma \leq 0$. The detailed symmetry analysis of this model is in the Supplementary Material (SM) Sec. I. [65]. We first discuss the case $\gamma = 0$, the Hermitian limit, in order to calculate the band structure and topological invariant.

Figure 1(c) shows the corresponding Brillouin Zone (BZ) of the honeycomb lattice. The dashed hexagon represents the first BZ, and we deform it into the rhomb in Fig. 1(c) for the following calculations [13]. The two bases of the k -space are labeled in Fig. 1(c). Each point in the k -space has a coordinate (k_1, k_2) . Figure 1(d) shows the band structure in the Hermitian limit and $\lambda = 0.4$. Since the unit cell contains 12 sites, this tight-binding model has 12 bands. When $\lambda = 0$, the model reduces to the direct sum of two subspaces, each describing a Wu-Hu model with a gapless double Dirac cone [25]. This means the interlayer couplings open the bandgap ΔE between the middle two bands, enabling the calculation of Wannier centers in the Hermitian limit, which are defined by the Wilson loop approach [13,24,66],

$$\hat{W}(k_1) = \prod_{i=1}^N \hat{M}(k_1, k_{2,i}, k_{2,i+1}). \quad (2)$$

In Eq. (2), $\hat{W}(k_1)$ represents the Wannier center matrix, which is the multiplication of the non-Abelian Berry connection matrices $\hat{M}(k_1, k_{2,i}, k_{2,i+1})$, whose matrix elements are written as,

$$\hat{M}(k_1, k_{2,i}, k_{2,i+1})_{nn'} = \langle u_n(k_1, k_{2,i}) | u_{n'}(k_1, k_{2,i+1}) \rangle. \quad (3)$$

In Eq. (3), $u_n(k_1, k_{2,i})$ is the periodical Bloch wavefunction for the n^{th} band. For a certain k_1 , the values of $k_{2,i}$ are sampled uniformly over the interval $[0, 2\pi]$ with $k_{2,1} = k_{2,N+1}$. Thus, all the $(k_1, k_{2,i})$ form a closed loop in the k -space. The dimension of $\hat{M}(k_1, k_{2,i}, k_{2,i+1})$ equals to the number of the valence bands, which is six. The Wannier centers $w_n(k_1)$ are associated with the eigenvalues $W_n(k_1)$ of the $\hat{W}(k_1)$ matrix,

$$w_n(k_1) = -\frac{1}{2\pi} \text{Im}(\log(W_n(k_1))). \quad (4)$$

The evolution of $w_n(k_1)$ is shown in Fig. 1(e). In the k -space, we examine the variation of $w_n(k_1)$ along the path from the Γ point ($k_1 = 0$) to the M point ($k_1 = \pi$). When λ is small, the adjacent Wannier bands either touch at the Γ point (2nd and 3rd, 4th and 5th bands) or the M point (1st and 2nd, 3rd and 4th, 5th and 6th bands), enabling a non-trivial \mathbb{Z}_2 topological invariant. As λ increases, the 1st and 2nd bands no longer degenerate at the M point and open a gap Δw , which is referred to as the Wannier gap. In Fig. 1(f), we mainly discuss the evolutions of ΔE and Δw as λ increases. Δw increases monotonically, whereas ΔE first increases then decreases. At $\lambda \approx 1.66$, the bandgap closes and won't open again as λ increases further, $\hat{W}(k_1)$ for the valence bands is not well-defined as well as the corresponding $w_n(k_1)$. Thus, the following discussion will mainly

focus on the range of λ where the bandgap exists.

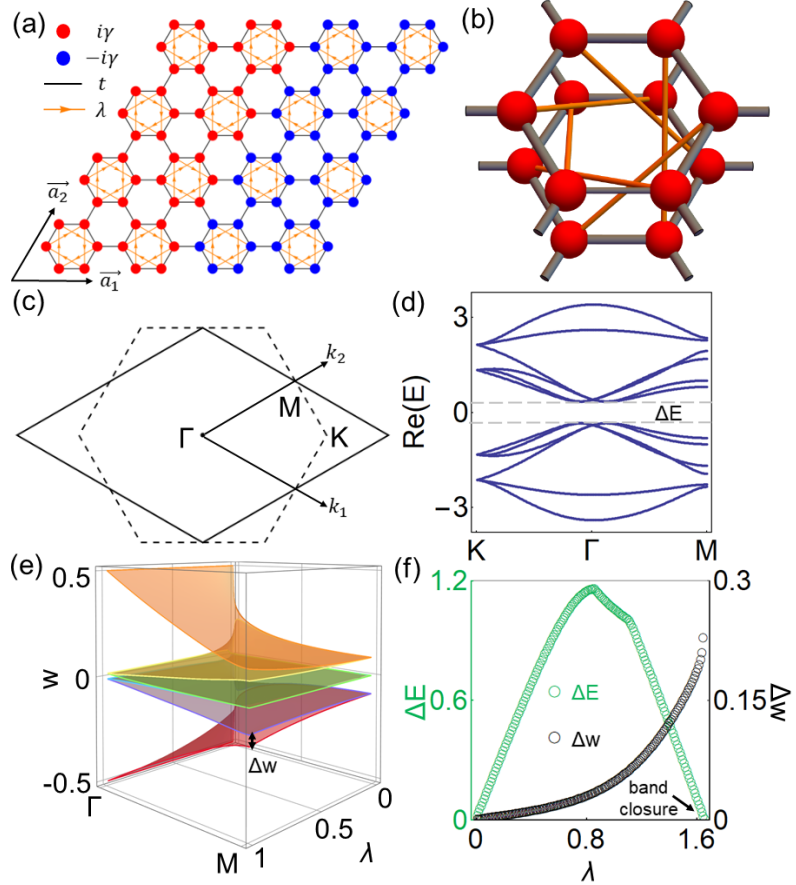


Fig. 1. (a) Schematic of the tight-binding model, the red (blue) circles represent gain (lossy) sites, the black lines are intralayer couplings, and the orange arrows represent interlayer couplings. \vec{a}_1 and \vec{a}_2 are the lattice vectors. γ, t and λ represent the gain-loss constant, intralayer and interlayer couplings, respectively. We set $t = 1$. (b) 3D ball-stick schematic of the unit cell. (c) The BZ of the honeycomb lattice, the dashed hexagon is the first BZ and the rhomb is the deformed BZ. \vec{k}_1 and \vec{k}_2 are the two bases. (d) Band structure of the tight-binding model in the Hermitian limit, and $\lambda = 0.4$. (e) The evolution of the Wannier centers in BZ with different λ , the Wannier gap Δw is labeled. (f) The evolution of bandgap ΔE (Green circles) and Wannier gap Δw (Black circles) with different λ .

For a finite system, each unit cell has a coordinate (m_1, m_2) , $m_1(m_2)$ represents the coordinate along the $\vec{a}_1(\vec{a}_2)$ -direction. Then we begin to discuss the projected band structure of the

bilayer breathing honeycomb lattice with a gain-loss domain wall. The \vec{a}_2 -direction is under PBC and the \vec{a}_1 -direction is finite with $2N$ unit cells. The sites with $m_1 \in [1, N]$ have on-site energies $i\gamma$ and sites with $m_1 \in [N+1, 2N]$ have on-site energies $-i\gamma$, and $\gamma = 1$. The boundary condition along the \vec{a}_1 -direction is presented in Fig. 2(a). Compared to Fig. 1(a), head-to-tail couplings are added along the \vec{a}_1 -direction, forming a cylinder geometry for the lattices which is called closed boundary condition (CBC) [56,57]. The reason to choose CBC instead of OBC along the \vec{a}_1 -direction is to diminish the effect of the higher-order topology [59,67–69], which will be discussed in SM. Sec. II [65]. We choose the interlayer coupling strength $\lambda = 0.4, 0.8$ and 1.2 , and present the corresponding projected band structures in Fig. 2(b)-(d), respectively. Edge states, shown in orange in Fig. 2(b)-(d), are induced on the gain-loss domain wall which are similar to the case of a Chern insulator with a gain-loss domain wall. As λ increases, the Wannier gap Δw becomes wider, and the edge states are no longer gapless. Moreover, in Fig. 2(d), the real dispersion of the edge states exhibits a flat band in a small interval, which is called the bulk Fermi arc [70]. Figures 2(e)-(g) are the corresponding complex energy spectra. We only present the spectra with $\text{Im}(E) < 0$ because the spectra with $\text{Im}(E) > 0$ can be inferred by the sublattice symmetry [35,71] (See detailed discussion in SM. Sec. I [65]). The spectra of edge states inside the real bandgap are also shown in orange, they form nondegenerate arcs in Fig. 2(e) and gradually become degenerate in Fig. 2(f) and (g). The reason for the nondegeneracy will be discussed in SM. Sec. I and II [65]. Moreover, the dispersion of the bulk states (gray lines in Fig. 2(b), (c), and (d)) indicates that the real bandgap does not increase monotonically as λ increases, but first increases then decreases, similar to the Hermitian case shown in Fig. 1(f).

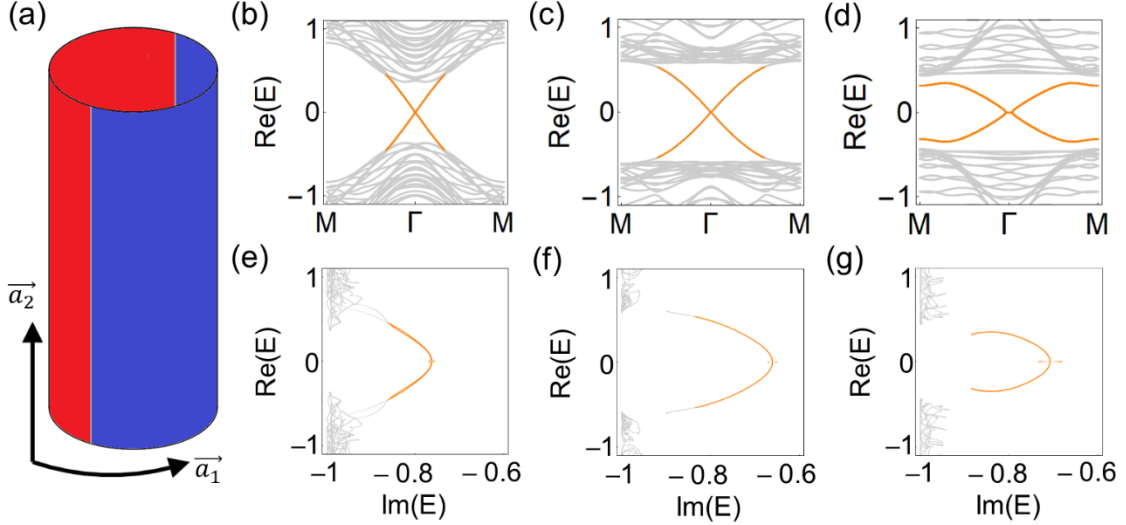


Fig. 2 (a) The bilayer breathing honeycomb lattices in a cylinder geometry (\vec{a}_1 -CBC/ \vec{a}_2 -PBC). The gain-loss domain wall is along the \vec{a}_2 -direction. (b), (c) and (d) are the real projected band structures for $\lambda = 0.4$, (b) $\lambda = 0.8$ (c) and $\lambda = 1.2$ (d), respectively. (e), (f) and (g) are the corresponding energy spectra with $\text{Im}(E) < 0$. The edge states inside the bandgap are shown in orange. Other parameters are set as $t = 1, N = 8$ and $\gamma = 1$.

In the next section, we discuss the HSTE of the edge states above by focusing on the eigenvalues and eigenstates under \vec{a}_1 -CBC/ \vec{a}_2 -OBC. The chiral edge states under the Hermitian limit transform into corner states by the insertion of a gain-loss domain wall, this phenomenon is also referred to as Non-Hermitian chiral skin effect [55–57]. The CBC along the \vec{a}_1 -direction induces two gain-loss domain walls, enabling slightly effective couplings [57] between the corner states localized at those two domain walls, which leads to the critical NHSE [72–74]. As the system size increases, the shape of corner states gradually approaches that of edge states. The spectra under \vec{a}_2 -PBC and \vec{a}_2 -OBC become increasingly similar and eventually overlap. Thus, we shall keep the system size invariant when tuning the value of the interlayer couplings to control the effect of critical NHSE. Figures 3(a)-(c) show the complex spectra of the strip system under \vec{a}_2 -PBC and finite lattices under \vec{a}_2 -OBC for (a) $\lambda = 0.4$, (b) $\lambda = 0.8$, and (c) $\lambda = 1.2$, respectively. Similar to Fig. 2(e)-(g), we present the spectra only with $\text{Im}(E) < 0$. The number of lattices along the \vec{a}_2 -direction $N_2 = 36$ and other parameters are equal to Fig. 2. Most of the eigenstates with the eigenvalues' real parts inside the real bandgap can be divided into two types, one type is the states localized at the top/bottom boundaries (Purple points in Fig. 3(a)-(c)), the other is the states localized

at the gain-loss domain walls (Red points in Fig. 3(a)-(c)). In the main text, we mainly discuss the latter, which corresponds to the edge states under \vec{a}_2 -PBC (Orange points in Fig. 3(a)-(c)) because the field distributions are both mainly localized at the domain walls. In SM. Sec. IV [65], we will discuss the field contributions of the purple points. Compared to Fig. 3(a)-(c), a straightforward phenomenon is the spectral difference between the orange and red points. As the increase of the interlayer couplings λ , the spectra of the domain wall states under \vec{a}_2 -PBC and \vec{a}_2 -OBC become more similar in Fig. 3(a)-(c), reflecting the suppression of HSTE from the eigenvalue's perspective. Moreover, we will present a semi-quantitative result in SM. Sec. III [65] about the evolution of the spectral difference in the interval of $\lambda \in [0.4, 1.2]$, it exhibits an overall decreasing trend and does not possess a clearly increasing interval. Compared to the result in Fig. 1(f), the evolution of the spectral difference in this interval more closely mirrors the evolution of the inverse of Wannier gap $1/\Delta w$ than the evolution of the bandgap ΔE . Figures 3(d)-(f) are the typical field distributions of the upper-layer for an eigenstate that belongs to the red points. The eigenstates of Fig. 3(d) and (e) are localized at the corners of the domain walls (labeled by black hexagrams), reflecting the nature of corner states. On the contrary, the eigenstate in Fig. 3(f) is a typical edge state on the domain wall. To make an effort in describing the HSTE from the eigenstate's perspective, we define the boundary density [57] $\sigma_i(m_2)$ for the i^{th} eigenstate ψ_i with eigenvalue E_i that belongs to the red points.

$$\sigma_i(m_2) = \sum_{\alpha \in \{\uparrow, \downarrow\}} \sum_{m_3 \in [1, 6]} \sum_{m_1 \in \{N, N+1\}} |\psi_i(\alpha, m_1, m_2, m_3)|^2. \quad (5)$$

In Eq. (5), m_3 is the index of the site in the unit cell of a single layer with $m_3 \in [1, 6]$. For each ψ_i , We extract the field distribution of the middle gain-loss domain wall, $m_1 \in \{N, N+1\}$ to calculate the boundary density $\sigma_i(m_2)$, and the eigenstates are chosen according to the $N_0 = 72$ smallest $|\text{Im}(E_i)|$ s. And the results of boundary densities are shown in Fig. 3(g), (h) and (i). For $\lambda = 0.4$ and 0.8 in Fig. 3(g) and (h), all the maxima of $\sigma_i(m_2)$ are at the edge, indicating that the corresponding eigenstates are skin corner states. However, for $\lambda = 1.2$ in Fig. 3(i), some eigenstates' maxima of boundary densities are in the bulk, reflecting the nature of edge states. The results show that some skin corner states change into edge states as λ increases, indicating the suppression of HSTE.

However, it is indirect to extract the quantitative relationship between the suppression of HSTE and the Wannier gap from the perspective of eigenstates. The main reason is the objective challenges

in quantitatively describing the NHSE from the perspective of eigenstates. For a skin corner state ψ_i , if its maximum of the $\sigma_i(m_2)$ locates on $\sigma_i(1)$, then we will have a qualitative relation $\sigma_i(m_2) \sim e^{-\kappa_i m_2}$ near $m_2 = 1$, $\kappa_i > 0$ represents the inverse decay length. The challenge is that NHSE is not the only reason for the emergence of the nonzero κ_i when the boundary condition along the \vec{a}_2 -direction changes from PBC to OBC. We need to consider the characteristics of the 2D Hermitian topological insulator and chiral edge states [1–3]. The eigenvalues of the chiral edge states under half-PBC are gapless, which means they fill the entire bandgap and become continuous in the thermodynamic limit. When the boundary condition changes from half-PBC to OBC, the eigenvalues in the bandgap remain invariant, and the field distribution of the chiral edge states is expected to extend along all edges and to decay exponentially from the edge into the bulk. For the bilayer breathing honeycomb lattices in the Hermitian limit, the features also exist when λ is small, such as Fig. S2 in SM. Sec. II [65]. If we still use Eq. (5) to check $\sigma_i(m_2)$, the qualitative relation should still hold for $\sigma_i(m_2)$ near $m_2 = 1$ with $\kappa_i > 0$ under \vec{a}_1 -OBC/ \vec{a}_2 -OBC due to the characteristic of chiral edge states. For the chiral edge state under \vec{a}_1 -OBC/ \vec{a}_2 -PBC, the Bloch theorem enables $\sigma_i(m_2)$ to be uniform for every m_2 , and $\kappa_i = 0$. The change of the boundary condition along the \vec{a}_2 -direction also leads to the change of the inverse decay length of $\sigma_i(m_2)$, which is not an exclusive characteristic of NHSE. Thus, for the skin corner states in the Non-Hermitian system, κ_i is qualitatively affected by two phenomena, one is NHSE, the other is the inverse decay length of chiral edge states in the Hermitian limit that is proportional to the bandgap ΔE [1–3]. When the interlayer coupling term λ increases, the bandgap ΔE will also change, so the change of κ_i will not directly relate to the suppression of HSTE. To summarize, evidence for the suppression of the HSTE, from the perspective of eigenstates, is manifested in the transition from corner states into edge states in Fig. 3(g-i). This phenomenon has not been observed when a finite gain-loss domain wall is inserted into a finite system with a bandgap and a stable topological invariant such as the Chern insulators [55–57]. Therefore, we have reason to believe that the emergence of edge states in Fig. 3(i) has a qualitative, potential relationship with fragile topology and the Wannier gap Δw , but the quantitative relationship between κ_i , ΔE and Δw still needs further study.

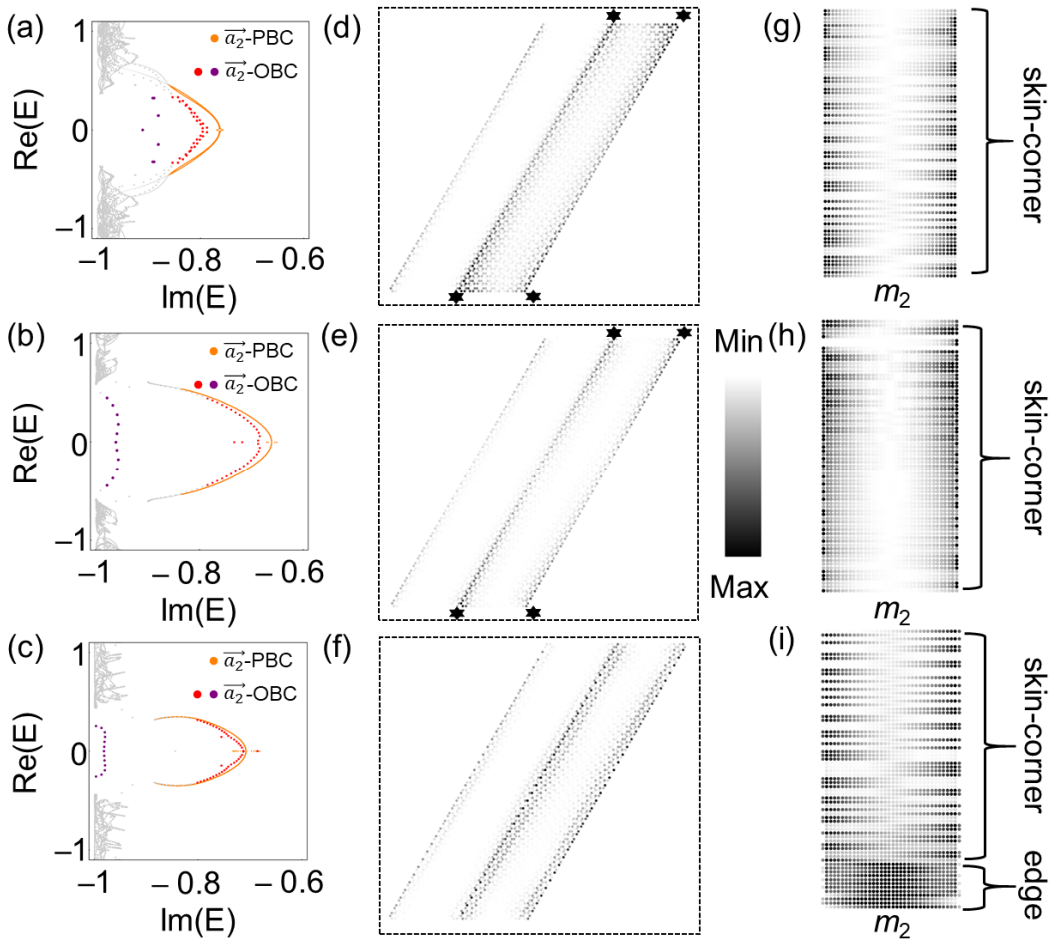


Fig. 3. (a), (b) and (c) are the complex spectra of strip system under \vec{a}_2 -PBC and finite lattices under \vec{a}_2 -OBC with $N_2 = 36$. Only spectra with $\text{Im}(E) < 0$ are shown, and the interlayer couplings are (a) $\lambda = 0.4$, (b) $\lambda = 0.8$ and (c) $\lambda = 1.2$, respectively. Orange points are the edge states induced by the domain wall under \vec{a}_2 -PBC, red points represent the states mainly localized at the domain walls under \vec{a}_2 -OBC, and the purple points are the states localized at the top and bottom boundaries under \vec{a}_2 -OBC. (d), (e) and (f) are the upper layer's field distributions about typical eigenstates which belong to the red points in (a), (b), and (c), respectively. The eigenstates in (d) and (e) are corner states, while the eigenstate in (f) is an edge state. The eigenvalues are (d) $E = 0.018 - 0.796i$ (e) $E = 0.016 - 0.687i$ (f) $E = 0.005 - 0.713i$. (g), (h) and (i) are the boundary densities for the eigenstates under \vec{a}_2 -OBC which are chosen according to the $N_0 = 72$ smallest $|\text{Im}(E_i)|$ s. Other parameters are the same as Fig. 2.

In summary, we provide potential evidence for the relationship between the suppression of

HSTE and fragile topology. As the interlayer coupling term of the bilayer breathing honeycomb lattice increases, the Wannier gap Δw becomes wider, and the spectral difference between \vec{a}_1 -CBC/ \vec{a}_2 -OBC and \vec{a}_1 -CBC/ \vec{a}_2 -PBC has an overall decreasing trend. Moreover, we can observe some skin corner states under \vec{a}_1 -CBC/ \vec{a}_2 -OBC change into edge states. The setup in this manuscript is quite experimental-friendly since the Hamiltonian only contains real couplings and on-site gain and loss. The closed boundary condition can be achieved in electric circuits [75] and transmission line networks [76]. Our findings offer possible phenomena of fragile topology, and explore new non-Hermitian phenomena in (higher-order) topological insulators and semimetals.

Acknowledgment

This work was supported by the National Natural Science Foundation of China (Grants No. 12334015, No. 12274332 and No. 12321161645), the National Key Research and Development Program of China (Grant No. 2022YFA1404900), the Key Research and Development Program of the Ministry of Science and Technology (Grants No. 2024YFB2808200).

Reference

- [1] M. Z. Hasan and C. L. Kane, *Colloquium* : Topological insulators, *Rev. Mod. Phys.* **82**, 3045 (2010).
- [2] X.-L. Qi and S.-C. Zhang, Topological insulators and superconductors, *Rev. Mod. Phys.* **83**, 1057 (2011).
- [3] S.-Q. Shen, *Topological Insulators*, Vol. 187 (Springer Singapore, Singapore, 2017).
- [4] K. V. Klitzing, G. Dorda, and M. Pepper, New Method for High-Accuracy Determination of the Fine-Structure Constant Based on Quantized Hall Resistance, *Phys. Rev. Lett.* **45**, 494 (1980).
- [5] D. J. Thouless, M. Kohmoto, M. P. Nightingale, and M. Den Nijs, Quantized Hall Conductance in a Two-Dimensional Periodic Potential, *Phys. Rev. Lett.* **49**, 405 (1982).
- [6] D. Xiao, M.-C. Chang, and Q. Niu, Berry phase effects on electronic properties, *Rev. Mod. Phys.* **82**, 1959 (2010).
- [7] F. D. M. Haldane, Model for a Quantum Hall Effect without Landau Levels: Condensed-Matter Realization of the “Parity Anomaly,” *Phys. Rev. Lett.* **61**, 2015 (1988).
- [8] B. A. Bernevig, T. L. Hughes, and S.-C. Zhang, Quantum Spin Hall Effect and Topological Phase Transition in HgTe Quantum Wells, *Science* **314**, 1757 (2006).
- [9] C. L. Kane and E. J. Mele, Quantum Spin Hall Effect in Graphene, *Phys. Rev. Lett.* **95**, 226801 (2005).
- [10] H. C. Po, H. Watanabe, and A. Vishwanath, Fragile Topology and Wannier Obstructions, *Phys. Rev. Lett.* **121**, 126402 (2018).
- [11] A. Alexandradinata, J. Höller, C. Wang, H. Cheng, and L. Lu, Crystallographic splitting

theorem for band representations and fragile topological photonic crystals, *Phys. Rev. B* **102**, 115117 (2020).

[12] J. Ahn, S. Park, and B.-J. Yang, Failure of Nielsen-Ninomiya Theorem and Fragile Topology in Two-Dimensional Systems with Space-Time Inversion Symmetry: Application to Twisted Bilayer Graphene at Magic Angle, *Phys. Rev. X* **9**, 021013 (2019).

[13] H.-X. Wang, G.-Y. Guo, and J.-H. Jiang, Band topology in classical waves: Wilson-loop approach to topological numbers and fragile topology, *New J. Phys.* **21**, 093029 (2019).

[14] K. Y. Lee, S. Wong, S. Vaidya, T. A. Loring, and A. Cerjan, Classification of fragile topology enabled by matrix homotopy, *Phys. Rev. Research* **7**, 033235 (2025).

[15] Z.-D. Song, L. Elcoro, and B. A. Bernevig, Twisted bulk-boundary correspondence of fragile topology, *Science* **367**, 794 (2020).

[16] V. Peri, Z.-D. Song, M. Serra-Garcia, P. Engeler, R. Queiroz, X. Huang, W. Deng, Z. Liu, B. A. Bernevig, and S. D. Huber, Experimental characterization of fragile topology in an acoustic metamaterial, *Science* **367**, 797 (2020).

[17] Y. Wu, Z.-K. Lin, Y. Yang, Z. Song, F. Li, and J.-H. Jiang, Probing fragile topology with a screw dislocation, *arXiv:2405.02057*.

[18] Y. Yang, Y. F. Xu, T. Xu, H.-X. Wang, J.-H. Jiang, X. Hu, and Z. H. Hang, Visualization of a Unidirectional Electromagnetic Waveguide Using Topological Photonic Crystals Made of Dielectric Materials, *Phys. Rev. Lett.* **120**, 217401 (2018).

[19] C. He, X. Ni, H. Ge, X.-C. Sun, Y.-B. Chen, M.-H. Lu, X.-P. Liu, and Y.-F. Chen, Acoustic topological insulator and robust one-way sound transport, *Nat. Phys.* **12**, 1124 (2016).

[20] Y. Li, Y. Sun, W. Zhu, Z. Guo, J. Jiang, T. Kariyado, H. Chen, and X. Hu, Topological LC-circuits based on microstrips and observation of electromagnetic modes with orbital angular momentum, *Nat. Commun.* **9**, 4598 (2018).

[21] W. Liu, Z. Ji, Y. Wang, G. Modi, M. Hwang, B. Zheng, V. J. Sorger, A. Pan, and R. Agarwal, Generation of helical topological exciton-polaritons, *Science* **370**, 600 (2020).

[22] W. Liu, M. Hwang, Z. Ji, Y. Wang, G. Modi, and R. Agarwal, Z₂ Photonic Topological Insulators in the Visible Wavelength Range for Robust Nanoscale Photonics, *Nano Lett.* **20**, 1329 (2020).

[23] S. Barik, H. Miyake, W. DeGottardi, E. Waks, and M. Hafezi, Two-dimensionally confined topological edge states in photonic crystals, *New J. Phys.* **18**, 113013 (2016).

[24] M. B. De Paz, M. G. Vergniory, D. Bercioux, A. García-Etxarri, and B. Bradlyn, Engineering fragile topology in photonic crystals: Topological quantum chemistry of light, *Phys. Rev. Research* **1**, 032005 (2019).

[25] L.-H. Wu and X. Hu, Scheme for Achieving a Topological Photonic Crystal by Using Dielectric Material, *Phys. Rev. Lett.* **114**, 223901 (2015).

[26] S. Xu, Y. Wang, and R. Agarwal, Absence of Topological Protection of the Interface States in Z₂ Photonic Crystals, *Phys. Rev. Lett.* **131**, 053802 (2023).

[27] X.-X. Wang, T. Kariyado, and X. Hu, Comment on “Absence of Topological Protection of the Interface States in Z₂ Photonic Crystals,” *Phys. Rev. Lett.* **134**, 099301 (2025).

[28] S. Xu, Y. Wang, and R. Agarwal, Xu *et al.* Reply:, *Phys. Rev. Lett.* **134**, 099302 (2025).

[29] N. Hatano and D. R. Nelson, Localization Transitions in Non-Hermitian Quantum Mechanics, *Phys. Rev. Lett.* **77**, 570 (1996).

[30] M. V. Berry, Physics of Nonhermitian Degeneracies, *Czech. J. Phys.* **54**, 1039 (2004).

[31] I. Rotter, A non-Hermitian Hamilton operator and the physics of open quantum systems, *J. Phys. A* **42**, 153001 (2009).

[32] C. M. Bender and S. Boettcher, Real Spectra in Non-Hermitian Hamiltonians Having P T Symmetry, *Phys. Rev. Lett.* **80**, 5243 (1998).

[33] W. D. Heiss, The physics of exceptional points, *J. Phys. A* **45**, 444016 (2012).

[34] W. D. Heiss, Exceptional points of non-Hermitian operators, *J. Phys. A* **37**, 2455 (2004).

[35] K. Kawabata, K. Shiozaki, M. Ueda, and M. Sato, Symmetry and Topology in Non-Hermitian Physics, *Phys. Rev. X* **9**, 041015 (2019).

[36] K. Ding, G. Ma, M. Xiao, Z. Q. Zhang, and C. T. Chan, Emergence, Coalescence, and Topological Properties of Multiple Exceptional Points and Their Experimental Realization, *Phys. Rev. X* **6**, 021007 (2016).

[37] J. Doppler, A. A. Mailybaev, J. Böhm, U. Kuhl, A. Girschik, F. Libisch, T. J. Milburn, P. Rabl, N. Moiseyev, and S. Rotter, Dynamically encircling an exceptional point for asymmetric mode switching, *Nature* **537**, 76 (2016).

[38] F. K. Kunst, E. Edvardsson, J. C. Budich, and E. J. Bergholtz, Biorthogonal Bulk-Boundary Correspondence in Non-Hermitian Systems, *Phys. Rev. Lett.* **121**, 026808 (2018).

[39] V. M. Martinez Alvarez, J. E. Barrios Vargas, and L. E. F. Foa Torres, Non-Hermitian robust edge states in one dimension: Anomalous localization and eigenspace condensation at exceptional points, *Phys. Rev. B* **97**, 121401 (2018).

[40] S. Yao and Z. Wang, Edge States and Topological Invariants of Non-Hermitian Systems, *Phys. Rev. Lett.* **121**, 086803 (2018).

[41] S. Yao, F. Song, and Z. Wang, Non-Hermitian Chern Bands, *Phys. Rev. Lett.* **121**, 136802 (2018).

[42] K. Yokomizo and S. Murakami, Non-Bloch Band Theory of Non-Hermitian Systems, *Phys. Rev. Lett.* **123**, 066404 (2019).

[43] H.-Y. Wang, F. Song, and Z. Wang, Amoeba Formulation of Non-Bloch Band Theory in Arbitrary Dimensions, *Phys. Rev. X* **14**, 021011 (2024).

[44] K. Zhang, Z. Yang, and C. Fang, Correspondence between Winding Numbers and Skin Modes in Non-Hermitian Systems, *Phys. Rev. Lett.* **125**, 126402 (2020).

[45] N. Okuma, K. Kawabata, K. Shiozaki, and M. Sato, Topological Origin of Non-Hermitian Skin Effects, *Phys. Rev. Lett.* **124**, 086801 (2020).

[46] D. S. Borgnia, A. J. Kruchkov, and R.-J. Slager, Non-Hermitian Boundary Modes and Topology, *Phys. Rev. Lett.* **124**, 056802 (2020).

[47] C. H. Lee and R. Thomale, Anatomy of skin modes and topology in non-Hermitian systems, *Phys. Rev. B* **99**, 201103 (2019).

[48] Y. Ashida, Z. Gong, and M. Ueda, Non-Hermitian Physics, *Adv. Phys.* **69**, 249 (2020).

[49] F. Song, S. Yao, and Z. Wang, Non-Hermitian Skin Effect and Chiral Damping in Open Quantum Systems, *Phys. Rev. Lett.* **123**, 170401 (2019).

[50] D. Zou, T. Chen, W. He, J. Bao, C. H. Lee, H. Sun, and X. Zhang, Observation of hybrid higher-order skin-topological effect in non-Hermitian topoelectrical circuits, *Nat. Commun.* **12**, 7201 (2021).

[51] C. H. Lee, L. Li, and J. Gong, Hybrid Higher-Order Skin-Topological Modes in Nonreciprocal Systems, *Phys. Rev. Lett.* **123**, 016805 (2019).

[52] Y. Li, C. Liang, C. Wang, C. Lu, and Y.-C. Liu, Gain-Loss-Induced Hybrid Skin-Topological

Effect, Phys. Rev. Lett. **128**, 223903 (2022).

[53] W. Zhu and J. Gong, Hybrid skin-topological modes without asymmetric couplings, Phys. Rev. B **106**, 035425 (2022).

[54] W. Zhu and L. Li, A brief review of hybrid skin-topological effect, J. Phys. Condens. Matter **36**, 253003 (2024).

[55] D. Nakamura, K. Inaka, N. Okuma, and M. Sato, Universal Platform of Point-Gap Topological Phases from Topological Materials, Phys. Rev. Lett. **131**, 256602 (2023).

[56] X.-R. Ma, K. Cao, X.-R. Wang, Z. Wei, Q. Du, and S.-P. Kou, Non-Hermitian chiral skin effect, Phys. Rev. Research **6**, 013213 (2024).

[57] T.-R. Liu, T. Liu, and M. Xiao, Anomalous non-Hermitian skin effect of chiral boundary states, Phys. Rev. B **112**, L081112 (2025).

[58] G.-G. Liu et al., Localization of Chiral Edge States by the Non-Hermitian Skin Effect, Phys. Rev. Lett. **132**, 113802 (2024).

[59] R. Gladstein Gladstone, M. Jung, and G. Shvets, Spin-Polarized Fractional Corner Charges and Their Photonic Realization, Phys. Rev. Lett. **128**, (2022).

[60] X.-C. Sun, H. Chen, H.-S. Lai, C.-H. Xia, C. He, and Y.-F. Chen, Ideal acoustic quantum spin Hall phase in a multi-topology platform, Nat. Commun. **14**, 952 (2023).

[61] W. Deng, X. Huang, J. Lu, V. Peri, F. Li, S. D. Huber, and Z. Liu, Acoustic spin-Chern insulator induced by synthetic spin-orbit coupling with spin conservation breaking, Nat. Commun. **11**, 3227 (2020).

[62] Y. Yang, J. Lu, M. Yan, X. Huang, W. Deng, and Z. Liu, Hybrid-Order Topological Insulators in a Phononic Crystal, Phys. Rev. Lett. **126**, 156801 (2021).

[63] H. Zhao, X. Qiao, T. Wu, B. Midya, S. Longhi, and L. Feng, Non-Hermitian topological light steering, Science **365**, 1163 (2019).

[64] Y. Li, C. Fan, X. Hu, Y. Ao, C. Lu, C. T. Chan, D. M. Kennes, and Q. Gong, Effective Hamiltonian for Photonic Topological Insulator with Non-Hermitian Domain Walls, Phys. Rev. Lett. **129**, 053903 (2022).

[65] See Supplementary material in [URL] for more information about symmetry analysis, simulation results in the Hermitian limit, the evolution of the spectral difference, and extra results of the finite systems. The SM contains Refs. [10,12,14,15,17,25,35,40,41,56,57,59,60, 63,64,67,70-74].

[66] R. Yu, X. L. Qi, A. Bernevig, Z. Fang, and X. Dai, Equivalent expression of Z 2 topological invariant for band insulators using the non-Abelian Berry connection, Phys. Rev. B **84**, 075119 (2011).

[67] J. Noh, W. A. Benalcazar, S. Huang, M. J. Collins, K. P. Chen, T. L. Hughes, and M. C. Rechtsman, Topological protection of photonic mid-gap defect modes, Nat. Photonics **12**, 408 (2018).

[68] B. Xie, H.-X. Wang, X. Zhang, P. Zhan, J.-H. Jiang, M. Lu, and Y. Chen, Higher-order band topology, Nat. Rev. Phys. **3**, 520 (2021).

[69] W. A. Benalcazar, T. Li, and T. L. Hughes, Quantization of fractional corner charge in C n - symmetric higher-order topological crystalline insulators, Phys. Rev. B **99**, 245151 (2019).

[70] H. Zhou, C. Peng, Y. Yoon, C. W. Hsu, K. A. Nelson, L. Fu, J. D. Joannopoulos, M. Soljačić, and B. Zhen, Observation of bulk Fermi arc and polarization half charge from paired exceptional points, Science **359**, 1009 (2018).

- [71] A. Altland and M. R. Zirnbauer, Nonstandard symmetry classes in mesoscopic normal-superconducting hybrid structures, *Phys. Rev. B* **55**, 1142 (1997).
- [72] L. Li, C. H. Lee, S. Mu, and J. Gong, Critical non-Hermitian skin effect, *Nat. Commun.* **11**, 5491 (2020).
- [73] K. Yokomizo and S. Murakami, Scaling rule for the critical non-Hermitian skin effect, *Phys. Rev. B* **104**, 165117 (2021).
- [74] Z. Yang, K. Zhang, C. Fang, and J. Hu, Non-Hermitian Bulk-Boundary Correspondence and Auxiliary Generalized Brillouin Zone Theory, *Phys. Rev. Lett.* **125**, 226402 (2020).
- [75] T. Helbig, T. Hofmann, S. Imhof, M. Abdelghany, T. Kiessling, L. W. Molenkamp, C. H. Lee, A. Szameit, M. Greiter, and R. Thomale, Generalized bulk-boundary correspondence in non-Hermitian topoelectrical circuits, *Nat. Phys.* **16**, 747 (2020).
- [76] T. Jiang, C. Zhang, R.-Y. Zhang, Y. Yu, Z. Guan, Z. Wei, Z. Wang, X. Cheng, and C. T. Chan, Observation of non-Hermitian boundary induced hybrid skin-topological effect excited by synthetic complex frequencies, *Nat. Commun.* **15**, 10863 (2024).